

Electro- and photoluminescence imaging as fast screening technique of the layer uniformity and device degradation in planar perovskite solar cells

Cite as: J. Appl. Phys. **120**, 035702 (2016); <https://doi.org/10.1063/1.4956436>

Submitted: 11 April 2016 • Accepted: 27 June 2016 • Published Online: 20 July 2016

Arman Mahboubi Soufiani, Murad J. Y. Tayebjee, Steffen Meyer, et al.



View Online



Export Citation



CrossMark

ARTICLES YOU MAY BE INTERESTED IN

[Detailed Balance Limit of Efficiency of p-n Junction Solar Cells](#)

Journal of Applied Physics **32**, 510 (1961); <https://doi.org/10.1063/1.1736034>

[Unusual defect physics in CH₃NH₃PbI₃ perovskite solar cell absorber](#)

Applied Physics Letters **104**, 063903 (2014); <https://doi.org/10.1063/1.4864778>

[Verification and mitigation of ion migration in perovskite solar cells](#)

APL Materials **7**, 041111 (2019); <https://doi.org/10.1063/1.5085643>



Webinar
Quantum Material Characterization
for Streamlined Qubit Development



Zurich
Instruments

Register now



Electro- and photoluminescence imaging as fast screening technique of the layer uniformity and device degradation in planar perovskite solar cells

Arman Mahboubi Soufiani,^{1,a)} Murad J. Y. Tayebjee,¹ Steffen Meyer,² Anita Ho-Baillie,¹ Jae Sung Yun,¹ Rowan W. MacQueen,^{3,b)} Leone Spiccia,² Martin A. Green,¹ and Ziv Hameiri^{1,a)}

¹Australian Centre for Advanced Photovoltaics, School of Photovoltaic and Renewable Energy Engineering, University of New South Wales, Sydney, NSW 2052, Australia

²School of Chemistry, Monash University, Clayton, VIC 3800, Australia

³School of Chemistry, University of Sydney, Sydney, NSW 2006, Australia

(Received 11 April 2016; accepted 27 June 2016; published online 20 July 2016; publisher error corrected 26 July 2016)

In this study, we provide insights into planar structure methylammonium lead triiodide (MAPbI₃) perovskite solar cells (PSCs) using electroluminescence and photoluminescence imaging techniques. We demonstrate the strength of these techniques in screening relatively large area PSCs, correlating the solar cell electrical parameters to the images and visualizing the features which contribute to the variation of the parameters extracted from current density-voltage characterizations. It is further used to investigate one of the major concerns about perovskite solar cells, their long term stability and aging. Upon storage under dark in dry glovebox condition for more than two months, the major parameter found to have deteriorated in electrical performance measurements was the fill factor; this was elucidated via electroluminescence image comparisons which revealed that the contacts' quality degrades. Interestingly, by deploying electroluminescence imaging, the significance of having a pin-hole free active layer is demonstrated. Pin-holes can grow over time and can cause degradation of the active layer surrounding them. Published by AIP Publishing. [<http://dx.doi.org/10.1063/1.4956436>]

INTRODUCTION

In the last four years, the photovoltaic research community has seen the emergence of an astonishingly high performance, highly compositionally versatile, and easy to fabricate organic-inorganic lead halide perovskite semiconductor materials^{1–3} with promising efficiencies achieved above 20% recently.^{2,4} Amongst a variety of deposition techniques used for high performance perovskite solar cells (PSCs),^{4–8} the majority of research groups employ solution-processed methods for active layer deposition.^{4,7,9} However, solution-processing is prone to spatial variations of both the electrical and optical properties of thin films, particularly within a large area device.¹⁰ While there has been an enormous effort to improve device performance and understand the optoelectronic properties of the materials,^{11–13} less work is focussed on developing fast and reliable full device characterization methods which is required for this technology to rapidly move forward for commercialization purposes. High-resolution fluorescence mapping techniques^{14,15} are useful for analysing laboratory scale devices but require a long measurement time, which is not suitable for fast characterization of large-area devices. Therefore, fast characterization techniques, which facilitate resolution of possible device non-uniformities across a large area, are deemed necessary. Additionally, mapping techniques could also be used to analyse performance changes of

perovskite solar cells during their operational lifetime, in particular, as PSCs are still lacking sufficient long-term stability under environmental conditions.^{16,17} Thus, fast mapping techniques would be very useful to better understand the impact of local changes within the device on its overall performance.^{18,19} Identifying the sources of performance loss to improve device stability are of critical importance for the development of commercially deployable PSCs.²⁰

Electroluminescence (EL) and photoluminescence (PL) imaging characterization techniques have been vastly used to spatially investigate the efficiency limiting factors of partially and fully processed solar cells.^{21–23} By exploring the charge carrier radiative recombination properties, detailed information about the distribution of non-radiative recombination centres, resistive and optical losses in solar cells can be obtained.^{22–25} However, the application of these techniques in understanding the electrical properties of PSCs is still being developed.^{24–26}

Photoluminescence measurements are based on the detection of photons generated by radiative recombination of the photo-generated electron-hole pairs, the majority of them being in the form of free carriers in the MAPbI₃ layer.²⁷ The parallel competing mechanism for radiative recombination is non-radiative carrier recombination such as Shockley-Read-Hall recombination (SRH),^{28–30} surface recombination at the interface between the perovskite and the charge carrier selective contacts,³¹ and higher order excitation density dependent Auger recombination.³²

Electroluminescence is based on the detection of photons generated from radiatively recombined charge carriers which are electrically injected into the active layer (i.e.,

^{a)}Electronic addresses: armansoufiani@gmail.com and ziv.hameiri@gmail.com

^{b)}Current address: Institute for Nanospectroscopy, Helmholtz-Zentrum Berlin für Materialien und Energie GmbH, Albert-Einstein-Str. 15, 12489 Berlin, Germany

MAPbI₃) of the solar cell upon applying voltage bias to the contacts. Imaging of the spatial distribution of the EL intensity provides combined information regarding **carrier recombination and series resistance (R_s)**. EL imaging has been used as a robust stand-alone characterization tool³³ for characterization of a wide range of thin film solar cells such as copper indium gallium selenide (CIGS)²³ and organic solar cells.³⁴

We have **recently confirmed the validity of the generalised Planck's emission law (Eq. (1)) for PSCs using EL and PL imaging.**²⁴ The generalised Planck's law describes the exponential correlation between the quasi-Fermi energy splitting and the luminescence intensity.^{24,35} According to the **reciprocity theorem**³⁶

$$\phi_{em}(E, \vec{r}) = EQE_{PV}(E, \vec{r}) \phi_{bb}(E) \left[\exp\left(\frac{qV_j(\vec{r})}{k_B T}\right) - 1 \right], \quad (1)$$

where the EL intensity, $\phi_{em}(E, \vec{r})$, at any position across the solar cell, \vec{r} , and for photon energy, E , is proportional to the photovoltaic external quantum efficiency, $EQE_{PV}(E, \vec{r})$, **spectral photon density of a black body, $\phi_{bb}(E)$** , and the **internal junction voltage $V_j(\vec{r})$** . q , k_B , and T are unit charge, Boltzmann constant, and temperature in Kelvin, respectively. According to Planck's law, a constant junction voltage results in a constant EL intensity (for specific E). However, the time-dependent behaviour of PL and EL in PSCs in the order of tens of seconds and longer^{37–41} requires primary device stabilization (i.e., **preconditioning**) **via poling** (i.e., forward biasing) or light-soaking (LS) for this correlation to hold.²⁴ These imaging techniques have also been recently used to understand the influence of MAPbI₃ crystal size on device performance in mesoporous structure PSC.²⁵

In this study, we have exemplified the application of EL/PL imaging techniques for the detailed analysis of PSC performance by connecting the device electrical parameters to the features visualized in the corresponding spatially resolved luminescence images. Planar structure PSCs with glass/FTO/c-TiO₂/CH₃NH₃PbI₃/Spiro-OMeTAD/Au architecture were chosen for two reasons: (1) the interpretation of EL/PL images was expected to be less complex than for devices with a mesoporous structure having a light scattering layer; and (2) the degradation of planar structures has been less intensely investigated in the literature.⁴² Using this system, we have demonstrated the usefulness of EL/PL imaging for investigating the long-term performance of PSCs as the evolution of the solar cell electrical parameters is clearly reflected in the EL image.

EXPERIMENTAL METHODS

Materials

Chemicals were purchased from Alfa Aesar (lead iodide, 99.999%), Sigma-Aldrich (methylamine solution, hydriodic acid solution, 4-*tert*-butylpyridine, lithium bis(trifluoromethylsulfonyl)imide (LiTFSI)), and Luminescence Technology Corporation (2,2',7,7'-tetrakis-(*N,N*-di-4-methoxyphenylamino)-9,9'-spirobifluorene (Spiro-OMeTAD)) and used as received. Fluorine-doped tin oxide (FTO) glass (3.2 mm thick, 8 Ω sq⁻¹ sheet resistance) was purchased from Dyesol.

Ultraviolet-curable resin (XNR5516ZB1) was purchased from Nagase ChemteX Corporation. CH₃NH₃I was synthesized by mixing solutions of CH₃NH₂ (20 ml, 0.23 mol, 40 wt. % in water) and HI (10 ml, 76 mmol, 57 wt. % in water) in water (100 ml). After stirring for 1 h, all volatiles were removed on a rotary evaporator at 60 °C. The product was dried in high vacuum (10⁻⁵ bar) at 60 °C for 24 h.

Solar cell preparation

Device fabrication was performed according to a published procedure by Huang *et al.*⁹ in which the MAPbI₃ layer of the solar cells was deposited via a gas-assisted fast crystallisation technique. Briefly, a dense titanium dioxide (c-TiO₂) blocking layer was deposited on a clean fluorine-doped tin oxide (FTO) glass by spray pyrolysis of a Ti(acac)₂(ⁱPrO)₂ (bis(isopropoxide)bis(acetylacetonato) titanium(IV)) solution (1:9 Ti(acac)₂(ⁱPrO)₂:isopropanol) at 475 °C. After cooling down to room temperature, a perovskite film was formed by spin coating a solution of CH₃NH₃PbI₃ in dimethylformamide (45 wt. %, prepared from PbI₂ and CH₃NH₃I in a molar ratio of 1:1) at 6000 rpm for 30 s with the assistance of a nitrogen flow (60 psi) after 2.5 s. The substrate was then annealed at 100 °C on a hotplate for 10 min. After cooling down to room temperature, a Spiro-OMeTAD solution in chlorobenzene (containing 40.8 mg Spiro-OMeTAD, 3.25 mg lithium bis(trifluoromethylsulphonyl)imide in 7.8 μ l acetonitrile, and 16.8 μ l 4-*tert*-butylpyridine in 500 μ l chlorobenzene) was spin coated on the perovskite film, followed by thermal deposition of 80 nm of gold. The device was then encapsulated by a cover glass with ultraviolet-curable adhesive inside a nitrogen filled glove box according to a procedure of Han *et al.*⁴³ We note that all the devices used in this study were encapsulated so as to minimize the impact of oxidation and moisture on the prolonged measurements.

I-V characterization

The current density-voltage (J - V) measurements were performed under AM1.5G illumination (100 mW·cm⁻²) using an Oriel solar simulator (model 94023A) and Keithley 2400 source meter. The J - V measurements were made on a defined area using a 0.16 cm² mask with a circular aperture (4.5 mm in diameter). In all measurements, the voltage was swept between 1.2 and -0.1 V with a scan rate of **30 mV s⁻¹**. The J - V parameters and curves are provided in the supplementary material, Table S1 and Fig. S1,⁴⁴ respectively.

Steady-state photoluminescence measurement

Steady-state (time-integrated) photoluminescence (SSPL) was used to characterize the PL peak position and spectra broadening. SSPL measurements were performed with a 405 nm, 60 mW, 1.5 mm-diameter excitation beam, and a Si charge-coupled device (CCD) camera. A 442 nm long-pass filter was used to remove the excitation beam from detection.

Electroluminescence and photoluminescence imaging

For photoluminescence and electroluminescence imaging measurements, a commercial 1-mega-pixel silicon

charge-coupled device (CCD) camera (Princeton Instruments, Trenton, NJ, USA) was used to detect the luminescence signal. A 750–850 nm bandpass filter was used prior to the camera collection lens to exclusively detect the emission from the perovskite active layer. A 630 nm red LED was used as the excitation light source for photoluminescence measurements with low irradiance at the device surface, ca. 0.04 to 0.045 Suns-equivalent illumination intensity. The voltage bias was controlled by a Source Measurement Unit, Agilent Technologies, controlled via computer software. The whole imaging setup was located inside a light-blocking box.

RESULTS AND DISCUSSION

We first investigated **EL imaging** as an independent and fast (**equal or less than 1 s per image**) technique to understand the underlying reasons for variation of the electrical properties between identically fabricated perovskite devices. Considering Eq. (1), in polycrystalline semiconductors²³ such as organic-inorganic lead halide perovskites, where there is a grain-to-grain optoelectronic variation,^{14,15} EQE_{PV} incorporates the variation of carrier recombination and optical losses on a micrometer length scale. The resistive losses integrated into the junction voltage are also spatially variable ($V_j = V_a - R_s \times I$, where V_a is the applied voltage at the terminals, R_s is total series resistance, and I is the dark injected current). Luminescence emission detected within a pixel in

these imaging techniques is performed on macroscopic scales and commonly averaged over small fraction of few square millimeters, which ideally allows the assumption of the spatial independency of EQE_{PV} . As such, the exponential dependence of EL emission on voltage junction dominates the detected EL signal, implying the importance of voltage drop over resistive losses.²³ Here, a comparison between two arbitrarily chosen devices in the same batch, demonstrates the application of the spatially resolved EL imaging in linking the **extracted electrical parameters from J - V measurements to features observed in their luminescence maps**.

Fig. 1(a) shows the relative difference in the electrical parameters of Cell 2 with respect to Cell 1 measured under forward and reverse voltage sweep directions. While the short-circuit current density (J_{SC}) of the two devices is very similar, indicating comparable active layer thickness and carrier collection efficiency, the fill factor (FF) shows the biggest relative difference among the electrical parameters with Cell 2 having an approximately 7% higher FF than Cell 1. Moreover, the FF of both devices is rather low compared to non-encapsulated devices with the same architecture and fabrication procedure. **A decrease in FF upon encapsulation is generally observed and is the subject of ongoing investigations**. In view of the slopes of the J - V curves of the two devices around the open-circuit voltage (V_{OC}) and J_{SC} (provided in Fig. S1), the major contribution to this **difference originates from R_s** , as shown in Fig. 1(a). To gain insights into the causes for the difference in solar

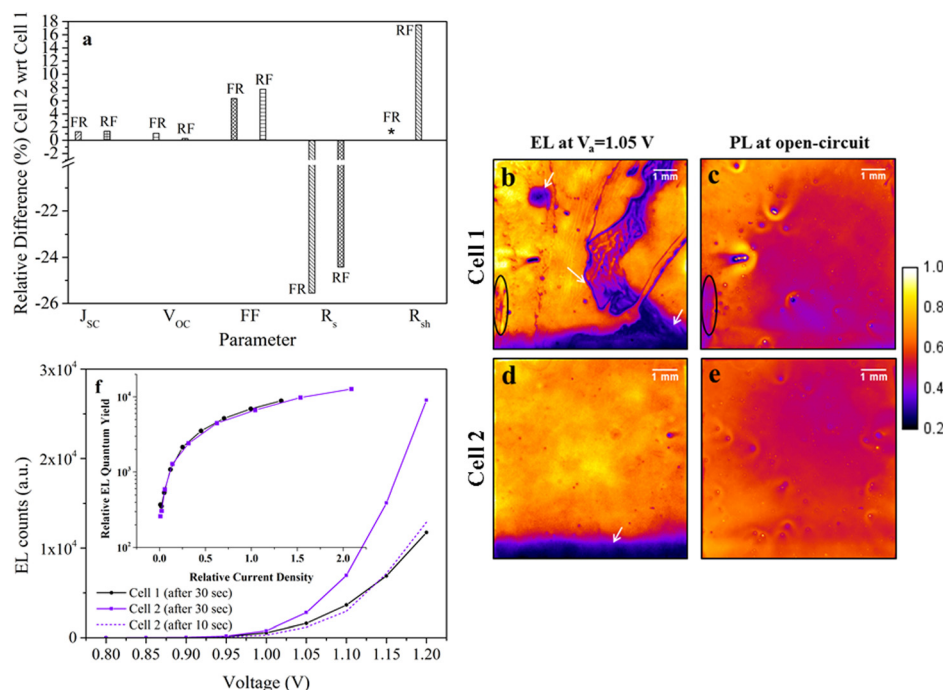


FIG. 1. (a) Relative difference in percent of the photovoltaic parameters of Cell 2 with respect to Cell 1 measured under $V_{OC} \rightarrow J_{SC}$ (FR) and $J_{SC} \rightarrow V_{OC}$ (RF) scan directions at a scan rate of 30 mV/s. The series resistance is obtained from the **slope of J - V curve near V_{OC}** . For absolute values of the device electrical parameters see Table S1. (b) and (d) EL images under forward voltage bias of 1.05 V for devices 1 and 2, respectively. (c) and (e) PL images obtained under 0.04 Suns-equivalent light intensity ($\approx 8 \times 10^{13} \text{ cm}^{-3}$ carrier density) at open-circuit condition for Cells 1 and 2, respectively. The intensity of all images is normalized to the maximum intensity. (f) Full-device averaged EL intensity evolution with voltage for Cells 1 and 2 (black line-circle and purple line-square curves, respectively), calculated from the images captured after 30 s of biasing initiation; Purple dashed curve shows the evolution of EL intensity for Cell 2 with images captured after 10 s. The inset depicts the relative quantum yield of the two devices with respect to their relative dark current density. *Using the linear fit approach to the J - V curve near the J_{SC} to extract the R_{sh} value for the FR scan direction, the calculated slope for both Cell 1 and Cell 2 had a very large error, thus the data were not included in the plot.

cell performance, the EL and PL images of both devices are investigated in detail.

Figures 1(b) and 1(c) present an EL image of Cell 1 under 1.05 V forward voltage bias and a PL image under open-circuit conditions (PL_{OC}), respectively. Figures 1(d) and 1(e) show the corresponding images of Cell 2. The spatial variation in PL_{OC} intensity commonly reflects the effective (i.e., bulk and surface) charge carrier recombination properties of the active layer material (i.e., MAPbI₃); a lower defect density results in a higher local voltage and brighter luminescence. As mentioned above, the EL signal is affected by the perovskite quality, shunting (e.g., when c-TiO₂ is in direct contact with the HTM), and also R_s . We note that severe shunting can also reduce the PL emission.

The more obvious, larger features are described first followed by the smaller features later in this section. The feature appearing as a dark strip at the bottom of the EL images of Cells 1 and 2 in Figs. 1(b) and 1(d) are near the isolation trench formed on the FTO-glass using laser scribe. The FTO layer is likely to be absent in this region and the underlying glass has experienced heat-induced damage before c-TiO₂ spray deposition,⁹ leading to a highly resistive region. These strips appear as an undistinguishably bright region under low-injection PL measurement (see Figs. 1(c) and 1(e)) demonstrating a negligible contribution of the perovskite layer to the feature. Photoluminescence images measured at short-circuit condition showed that these regions appear brighter than the rest of the device, supporting the notion that higher contact resistance in these regions inhibits efficient charge carrier extraction (see Fig. S2).

While the EL image of Cell 2 appears quite uniform (Fig. 1(d)), prominent features (dark color) can be seen in EL image of Cell 1 (see Fig. 1(b)). As shown by Rau *et al.*²³ on large scale Cu(In,Ga)Se₂ solar cells, features in EL images are predominately due to resistive losses, both series and shunt resistances, whereas abrupt drops in EL intensity are usually related to pronounced local shunting^{23,45} which is dependent on the injection-level. The circular (top left area indicated with white arrow) and the fissure-like smeared dark regions appearing in the EL image (Fig. 1(b)) of Cell 1 suggest that a highly resistive interlayer contact may exist which affects the EL but not the PL. We note that these features are likely to be a result of solution-based deposition of Spiro-OMeTAD rather than c-TiO₂. More information can be deduced from the plot of EL quantum yield versus injected dark current density. The initial part of such a plot, in a semi-logarithmic form, which shows steep slope in perovskite solar cells,²⁵ as illustrated in the inset of Fig. 1(f), is mainly dominated by the SRH recombination and shunting processes. We note that because the active area (i.e., deposited gold area) of the two devices are obtained from their EL images in equivalent resolution (i.e., pixel area), the current densities used in the inset of Fig. 1(f), and thus EL quantum yields, are presented in relative form by dividing the device-averaged EL counts by the corresponding relative current densities. No divergence between the curves associated with the two devices was found, in particular, at low current injection levels. Therefore, the attribution of the features in the EL images of Cell 1 (Fig. 1(b)) to shunting can be

thoughtfully ruled out. In addition, if severe shunting existed, the abovementioned dark features would be observed in the PL_{OC} image (Fig. 1(c)). A possible explanation for the large dark features in the EL image of Cell 1 is that they are regions with an anomalously thin Spiro-OMeTAD layer, resulting in anomalously high sheet resistance, contributing to the total FF loss due to R_s of the device. The marginal difference in the relative EL quantum yield of the two devices, within the photovoltaic voltage working regime, corresponds well with the very similar V_{OC} of both devices (see Fig. 1(a)).

The dark scratch-like feature appearing at bottom-left side in both PL and EL images of Cell 1 (indicated with black oval in Figures 1(b) and 1(c)) represents most likely a region with damaged perovskite layer which in turn reduces the photo and electro-injected charge carriers concentration (i.e., reduces internal voltage).

The outcome of the EL mapping of the two solar cells is consistent with the results from J - V characterisation where the difference between the two devices mostly originates from the higher R_s of Cell 1 compared to Cell 2. This demonstrates the strength of the EL imaging technique in obtaining a comprehensive understanding of the performance limitations of PSCs within short time. To support the interpretations of Fig. 1, similar analysis using the information extractable from EL imaging is provided in Fig. S3 for two other solar cells fabricated following an identical procedure but from a different batch of precursors.

As an important side note, when comparing the EL intensity of different devices it is essential to collect the images after a fixed time of voltage bias initiation. For example, the images collected after 10 s for Cell 2 (dashed purple curve in Fig. 1(f)) should not be compared to the image after 30 s for Cell 1 (black curve in Fig. 1(f)) as the EL intensity strongly increases with time.

Cell 2 was further used for investigating possible long-term changes in the EL/PL intensity upon storage in nitrogen atmosphere in the dark for two months. Fig. 2(a) shows the J - V curves for Cell 2, fresh and aged. A summary of the changes in the electrical parameters of the device for the $V_{OC} \rightarrow J_{SC}$ (i.e., FR) sweep direction is included in the inset table of Fig. 2(a). J - V measurements were done following identical procedure for the fresh and aged sample in order to exclude any undesirable effect caused by preconditioning of the solar cell.⁴⁶ The least variation was observed in V_{OC} after two months suggesting a minimal change to the bulk properties of the perovskite layer. This is consistent with the unchanged peak position at ~ 773 nm and full-width at half maximum of the spectral PL of the fresh and aged device (see Fig. 2(f)). The largest contribution to the power conversion efficiency reduction originated from the decrease in FF by $\sim 10\%$. To establish whether the change in device performance had an effect on the luminescence, EL images were collected at 1.05 V forward voltage bias (Figs. 2(b) and 2(c)) and PL images at open-circuit (Fig. 2(e)). By comparing the EL intensities of Figs. 2(b) and 2(c) several findings are obvious: The small dark spots identified in Fig. 2(b) which are ascribed to pinholes—confirmed by the optical microscope image shown in Fig. S3—have grown over time as evident

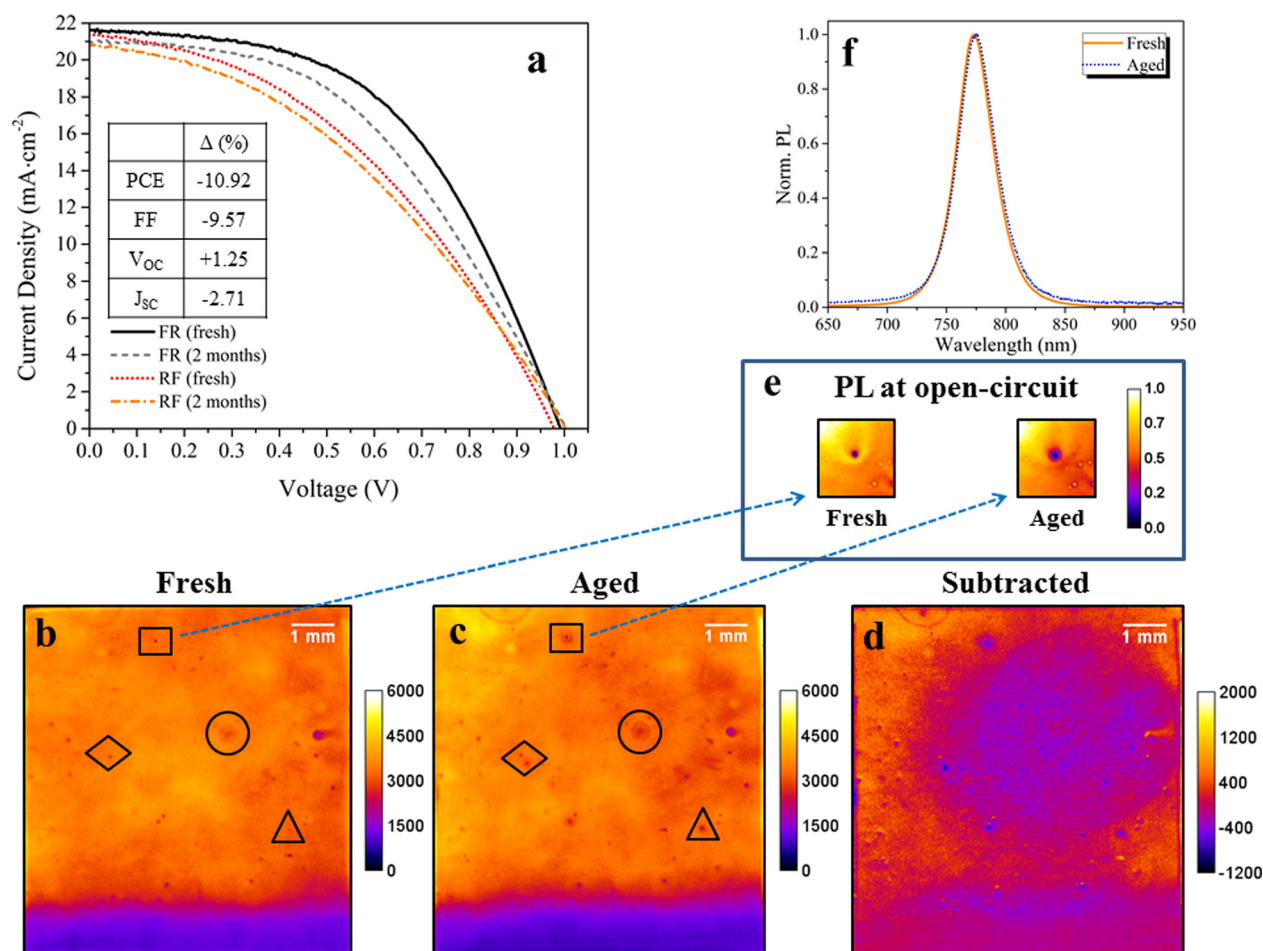


FIG. 2. (a) J - V characteristic curves of the fresh and two-months aged Cell 2 (stored in dark in glovebox); the inset table shows the change in the electrical parameters in percentage for the FR sweep direction. (b) and (c) The corresponding EL images of fresh and two-months aged device, respectively, both voltage biased at 1.05 V. **Images are collected after 30 s of bias initiation**; the calibration bar shows the actual intensities in arbitrary units. The inset (e) displays the normalized PL_{OC} images of the spot enclosed in a rectangle in part 2b and 2c. (d) Subtracted image of the fresh device from the aged device. (f) Normalized spectral PL of the fresh and aged solar cell.

from the EL image of the aged device in Fig. 2(c). As a result, some new spots became visible within the resolution of the EL image upon aging. Importantly, not only are the pinholes growing in size but it also seems that the **surrounding MAPbI₃ degrades over time**. This is exemplified in the zoomed-in PL_{OC} images (Fig. 2(e)) of the spot identified with a rectangle in Figs. 2(b) and 2(c). The PL images also confirm the growth of the same pinhole discussed above. Although the underlying mechanism of the pinhole growth and its surrounding degradation is not clear yet, its contribution to device performance is expected to be more likely a reduction in shunt resistance or an increase in ideality factor rather than influencing series resistance. However, since the V_{OC} does not degrade over time, the increased shunting effect is minimal and only observed as a reduced FF . Nevertheless, these findings highlight the importance of fabricating pinhole-free perovskite layers.⁴⁷ Another intriguing observation is that in addition to the inhomogeneous aging of the planar PSC, some regions of the device, for instance, the top-left side, **show improved EL intensity over time**. A clearer picture is obtained by subtraction of the EL image of the fresh device from that of aged, shown in Fig. 2(d). A possible explanation for the EL enhancement in some parts of

the device could be the **shift in the current flow from the surrounding regions with higher local series resistance towards these more accessible regions**. This explanation implies that it is unnecessary to invoke a change in the bulk material quality in the brighter EL regions, and this is consistent with the **unchanged V_{OC}** (Table inset in Fig. 2(a)). It is evident from the **subtracted image that the major part of the EL image has decreased in intensity over time**. By comparing this finding with the data obtained from J - V measurements (i.e., FF), it can be concluded that the **EL images are dominated by resistance losses**, suggesting that the performance loss upon aging mainly originates from changes of the perovskite/Spiro-OMeTAD and/or perovskite/c-TiO₂ interfaces affecting the R_s . Several studies have been dedicated to the understanding of the degradation mechanisms of neat MAPbI₃ films and its corresponding solar cells and the device stability improvement under different conditions.^{37,43,48–52} Although the devices were stored in the dark in N₂-environment of a glovebox with a very low levels of O₂ (≈ 1 ppm) and H₂O (< 1 ppm), partial degradation of the perovskite layer from trace amounts cannot be fully excluded. The decrease in device performance may also be initiated by the very first J - V measurements and/or the forward biasing of the solar cell

for EL imaging measurements. In both cases, the device experiences an electric field which was recently reported by Carrillo *et al.* to affect the charge selective contact layers.⁵³ Although no long-term study was conducted in their work, it was proposed that under electric-field the mobile ions in MAPbI₃ (i.e., mainly iodine ion⁵⁴) move towards the charge selective contacts⁵⁵ and react reversibly with TiO₂ and irreversibly with Spiro-OMeTAD.⁵³ The latter permanent reaction was suggested to progressively deteriorate the conductivity of the Spiro-OMeTAD and affect the solar cell long-term performance, which is consistent with our observation of the FF degradation.

Notably, the subtracted EL image in Figure 2(d) reveals another feature: A dark circular area, 4.5 mm in diameter, which corresponds to the region where the device was illuminated during *J-V* characterisation using a round 0.16 cm² shadow mask. This fingerprint left after the *J-V* scan is to a large extent reversible, fading away after several hours,²⁴ whereas the image in Fig. 2(b) was collected 6 h after the *J-V* measurement on the device. The mechanism behind the reversible illumination induced change in luminescence intensity, visible even several hours after light exposure, is unclear at this stage, but our investigations are ongoing.

CONCLUSIONS

The application of fast and spatially resolved PL and EL full-device imaging techniques to perovskite solar cells is in its developing stage. In this work, detailed analyses of the luminescence images of planar solar cells were performed to link the electrical parameters obtained from common current density-voltage measurements to the features observed in the spatially resolved luminescence images, in particular, EL images. Using EL imaging, it was further shown that pinholes are likely to act as a source of increased degradation over time even when devices were stored in a dry glovebox environment, pointing to the importance of developing pinhole free solar cells. Moreover, EL imaging is revealed to be a suitable technique to investigate the effect of reversible illumination induced changes in the device.

ACKNOWLEDGMENTS

The authors thank Anastasia Soeriyadi for assistance in taking the optical microscope image. The authors acknowledge support from the Australian Government through the Australian Renewable Energy Agency (ARENA, Project No. 2014/RND097) and the Australian Centre for Advanced Photovoltaics (ACAP). The views expressed herein are not necessarily the views of the Australian Government, and the Australian Government does not accept responsibility for any information or advice contained herein. Z.H. acknowledges the support of the Australian Research Council (ARC) through the Discovery Early Career Researcher Award (DECRA, Project No. DE150100268) while S.M. gratefully acknowledges the Alexander von Humboldt Foundation for a Feodor Lynen Research Fellowship.

- ²M. A. Green, K. Emery, Y. Hishikawa, W. Warta, and E. D. Dunlop, "Solar cell efficiency tables (version 46)," *Prog. Photovoltaics* **23**, 805–812 (2015).
- ³A. Kojima, K. Teshima, Y. Shirai, and T. Miyasaka, "Organometal halide perovskites as visible-light sensitizers for photovoltaic cells," *J. Am. Chem. Soc.* **131**, 6050–6051 (2009).
- ⁴N. J. Jeon, J. H. Noh, W. S. Yang, Y. C. Kim, S. Ryu, J. Seo, and S. I. Seok, "Compositional engineering of perovskite materials for high-performance solar cells," *Nature* **517**, 476–480 (2015).
- ⁵Q. Chen, H. Zhou, Z. Hong, S. Luo, H.-S. Duan, H.-H. Wang, Y. Liu, G. Li, and Y. Yang, "Planar heterojunction perovskite solar cells via vapor assisted solution process," *J. Am. Chem. Soc.* **136**, 622–625 (2014).
- ⁶M. Liu, M. B. Johnston, and H. J. Snaith, "Efficient planar heterojunction perovskite solar cells by vapour deposition," *Nature* **501**, 395–398 (2013).
- ⁷J. Burschka, N. Pellet, S.-J. Moon, R. Humphry-Baker, P. Gao, M. K. Nazeeruddin, and M. Gratzel, "Sequential deposition as a route to high-performance perovskite-sensitized solar cells," *Nature* **499**, 316–319 (2013).
- ⁸J. H. Heo, S. H. Im, J. H. Noh, T. N. Mandal, C.-S. Lim, J. A. Chang, Y. H. Lee, H.-j. Kim, A. Sarkar, Md. K. Nazeeruddin *et al.*, "Efficient inorganic-organic hybrid heterojunction solar cells containing perovskite compound and polymeric hole conductors," *Nat. Photonics* **7**, 486–491 (2013).
- ⁹F. Huang, Y. Dkhissi, W. Huang, M. Xiao, I. Benesperi, S. Rubanov, Y. Zhu, X. Lin, L. Jiang, and Y. Zhou, "Gas-assisted preparation of lead iodide perovskite films consisting of a monolayer of single crystalline grains for high efficiency planar solar cells," *Nano Energy* **10**, 10–18 (2014).
- ¹⁰G. Brown, A. Pudov, B. Cardozo, V. Faifer, E. Bykov, and M. Contreras, "Quantitative imaging of electronic nonuniformities in Cu (In, Ga) Se₂ solar cells," *J. Appl. Phys.* **108**, 074516 (2010).
- ¹¹S. D. Stranks, G. E. Eperon, G. Grancini, C. Menelaou, M. J. P. Alcocer, T. Leijtens, L. M. Herz, A. Petrozza, and H. J. Snaith, "Electron-hole diffusion lengths exceeding 1 micrometer in an organometal trihalide perovskite absorber," *Science* **342**, 341–344 (2013).
- ¹²M. A. Green, Y. Jiang, A. Mahboubi Soufiani, and A. W.-Y. Ho-Baillie, "Optical properties of photovoltaic organic-inorganic lead halide perovskites," *J. Phys. Chem. Lett.* **6**, 4774–4785 (2015).
- ¹³B. Chen, M. Yang, X. Zheng, C. Wu, W. Li, Y. Yan, J. Bisquert, G. Garcia-Belmonte, K. Zhu, and S. Priya, "Impact of capacitive effect and ion migration on the hysteretic behavior of perovskite solar cells," *J. Phys. Chem. Lett.* **6**, 4693–4700 (2015).
- ¹⁴D. W. de Quilettes, S. M. Vorpahl, S. D. Stranks, H. Nagaoka, G. E. Eperon, M. E. Ziffer, H. J. Snaith, and D. S. Ginger, "Impact of microstructure on local carrier lifetime in perovskite solar cells," *Science* **348**, 683–686 (2015).
- ¹⁵M. Vrućinić, C. Matthiesen, A. Sadhanala, G. Divitini, S. Cacovich, S. E. Dutton, C. Ducati, M. Atatüre, H. Snaith, R. H. Friend *et al.*, "Local versus long-range diffusion effects of photoexcited states on radiative recombination in organic-inorganic lead halide perovskites," *Adv. Sci.* **2**(9), 1500136 (2015).
- ¹⁶T. A. Berhe, W.-N. Su, C.-H. Chen, C.-J. Pan, J.-H. Cheng, H.-M. Chen, M.-C. Tsai, L.-Y. Chen, A. A. Dubale, and B.-J. Hwang, "Organometal halide perovskite solar cells: Degradation and stability," *Energy Environ. Sci.* **9**, 323–356 (2016).
- ¹⁷D. Wang, M. Wright, N. K. Elumalai, and A. Uddin, "Stability of perovskite solar cells," *Sol. Energy Mater. Sol. Cells* **147**, 255–275 (2016).
- ¹⁸M. Seeland, R. Rösch, and H. Hoppe, "Luminescence imaging of polymer solar cells: Visualization of progressing degradation," *J. Appl. Phys.* **109**, 064513 (2011).
- ¹⁹R. Rösch, D. M. Tanenbaum, M. Jorgensen, M. Seeland, M. Barenklau, M. Hermenau, E. Voroshazi, M. T. Lloyd, Y. Galagan, B. Zimmermann *et al.*, "Investigation of the degradation mechanisms of a variety of organic photovoltaic devices by combination of imaging techniques—the ISOS-3 inter-laboratory collaboration," *Energy Environ. Sci.* **5**, 6521–6540 (2012).
- ²⁰M. A. Green, "Commercial progress and challenges for photovoltaics," *Nat. Energy* **1**, 15015 (2016).
- ²¹T. Trupke, B. Mitchell, J. Weber, W. McMillan, R. Bardos, and R. Kroeze, "Photoluminescence imaging for photovoltaic applications," *Energy Procedia* **15**, 135–146 (2012).
- ²²T. Trupke, R. Bardos, M. Schubert, and W. Warta, "Photoluminescence imaging of silicon wafers," *Appl. Phys. Lett.* **89**, 044107 (2006).
- ²³A. Helbig, T. Kirchartz, R. Schaeffler, J. H. Werner, and U. Rau, "Quantitative electroluminescence analysis of resistive losses in Cu (In,

¹M. A. Green, A. Ho-Baillie, and H. J. Snaith, "The emergence of perovskite solar cells," *Nat. Photonics* **8**, 506–514 (2014).

- Ga) Se₂ thin-film modules," *Sol. Energy Mater. Sol. Cells* **94**, 979–984 (2010).
- ²⁴Z. Hameiri, A. Mahboubi Soufiani, M. K. Juhl, L. Jiang, F. Huang, Y.-B. Cheng, H. Kampwerth, J. W. Weber, M. A. Green, and T. Trupke, "Photoluminescence and electroluminescence imaging of perovskite solar cells," *Prog. Photovoltaics* **23**, 1697–1705 (2015).
- ²⁵S. Mastroianni, F. D. Heinz, J. H. Im, W. Veurman, M. Padilla, M. C. Schubert, U. Würfel, M. Gratzel, N. G. Park, and A. Hinsch, "Analysing the effect of crystal size and structure in highly efficient CH₃NH₃PbI₃ perovskite solar cells by spatially resolved photo- and electroluminescence imaging," *Nanoscale* **7**, 19653–19662 (2015).
- ²⁶T. Handa, D. M. Tex, A. Shimazaki, T. Aharen, A. Wakamiya, and Y. Kanemitsu, "Optical characterization of voltage-accelerated degradation in CH₃NH₃PbI₃ perovskite solar cells," *Opt. Express* **24**, A917–A924 (2016).
- ²⁷A. M. Soufiani, F. Huang, P. Reece, R. Sheng, A. Ho-Baillie, and M. A. Green, "Polaronic exciton binding energy in iodide and bromide organic-inorganic lead halide perovskites," *Appl. Phys. Lett.* **107**, 231902 (2015).
- ²⁸S. D. Stranks, V. M. Burlakov, T. Leijtens, J. M. Ball, A. Goriely, and H. J. Snaith, "Recombination kinetics in organic-inorganic perovskites: Excitons, free charge, and subgap states," *Phys. Rev. Appl.* **2**, 034007 (2014).
- ²⁹X. Wen, Y. Feng, S. Huang, F. Huang, Y.-B. Cheng, M. Green, and A. Ho-Baillie, "Defect trapping states and charge carrier recombination in organic-inorganic halide perovskites," *J. Mater. Chem. C* **4**, 793–800 (2016).
- ³⁰W. Shockley and W. Read, Jr., "Statistics of the recombinations of holes and electrons," *Phys. Rev.* **87**, 835 (1952).
- ³¹Y. Shao, Z. Xiao, C. Bi, Y. Yuan, and J. Huang, "Origin and elimination of photocurrent hysteresis by fullerene passivation in CH₃NH₃PbI₃ planar heterojunction solar cells," *Nat. Commun.* **5**, 5784 (2014).
- ³²R. L. Milot, G. E. Eperon, H. J. Snaith, M. B. Johnston, and L. M. Herz, "Temperature-dependent charge-carrier dynamics in CH₃NH₃PbI₃ perovskite thin films," *Adv. Funct. Mater.* **25**, 6218–6227 (2015).
- ³³K. Bothe, P. Pohl, J. Schmidt, T. Weber, P. Altermatt, B. Fischer, and R. Brendel, "Electroluminescence imaging as an in-line characterisation tool for solar cell production," in *21st European Photovoltaic Solar Energy Conference, Dresden* (2006), pp. 597–600.
- ³⁴M. Seeland, R. Rösch, and H. Hoppe, "Quantitative analysis of electroluminescence images from polymer solar cells," *J. Appl. Phys.* **111**, 024505 (2012).
- ³⁵P. Würfel, "The chemical potential of radiation," *J. Phys. C: Solid State Phys.* **15**, 3967 (1982).
- ³⁶U. Rau, "Reciprocity relation between photovoltaic quantum efficiency and electroluminescent emission of solar cells," *Phys. Rev. B* **76**, 085303 (2007).
- ³⁷O. A. Jaramillo-Quintero, R. S. Sanchez, M. Rincon, and I. Mora-Sero, "Bright visible-infrared light emitting diodes based on hybrid halide perovskite with spiro-OMeTAD as a hole-injecting layer," *J. Phys. Chem. Lett.* **6**, 1883–1890 (2015).
- ³⁸K. Wojciechowski, S. D. Stranks, A. Abate, G. Sadoughi, A. Sadhanala, N. Kopidakis, G. Rumbles, C.-Z. Li, R. H. Friend, and A. K.-Y. Jen, "Heterojunction modification for highly efficient organic-inorganic perovskite solar cells," *ACS Nano* **8**, 12701–12709 (2014).
- ³⁹K. Wojciechowski, T. Leijtens, S. Siprova, C. Schlueter, M. T. Hörantner, J. T.-W. Wang, C.-Z. Li, A. K. Y. Jen, T.-L. Lee, and H. J. Snaith, "C60 as an efficient n-Type compact layer in perovskite solar cells," *J. Phys. Chem. Lett.* **6**, 2399–2405 (2015).
- ⁴⁰M. Okano, M. Endo, A. Wakamiya, M. Yoshita, H. Akiyama, and Y. Kanemitsu, "Degradation mechanism of perovskite CH₃NH₃PbI₃ diode devices studied by electroluminescence and photoluminescence imaging spectroscopy," *Appl. Phys. Express* **8**, 102302 (2015).
- ⁴¹B. Wu, K. Fu, N. Yantara, G. Xing, S. Sun, T. C. Sum, and N. Mathews, "Charge accumulation and hysteresis in perovskite-based solar cells: An electro-optical analysis," *Adv. Energy Mater.* **5**, 1500829 (2015).
- ⁴²A. Guerrero, J. You, C. Aranda, Y. S. Kang, G. Garcia-Belmonte, H. Zhou, J. Bisquert, and Y. Yang, "Interfacial degradation of planar lead halide perovskite solar cells," *ACS Nano* **10**, 218–224 (2016).
- ⁴³Y. Han, S. Meyer, Y. Dkhissi, K. Weber, J. M. Pringle, U. Bach, L. Spiccia, and Y.-B. Cheng, "Degradation observations of encapsulated planar CH₃NH₃PbI₃ perovskite solar cells at high temperatures and humidity," *J. Mater. Chem. A* **3**, 8139–8147 (2015).
- ⁴⁴See supplementary material at <http://dx.doi.org/10.1063/1.4956436> for more experimental details results, and discussions.
- ⁴⁵J. Raguse, J. T. McGoffin, and J. R. Sites, "Electroluminescence system for analysis of defects in CdTe cells and modules," in *2012 38th IEEE Photovoltaic Specialists Conference (PVSC)* (2012), pp. 000448–000451.
- ⁴⁶M. De Bastiani, G. Dell'Erba, M. Gandini, V. D'Innocenzo, S. Neutzner, A. R. S. Kandada, G. Grancini, M. Binda, M. Prato, and J. M. Ball, "Ion migration and the role of preconditioning cycles in the stabilization of the J–V characteristics of inverted hybrid perovskite solar cells," *Adv. Energy Mater.* **6**, 1501453 (2015).
- ⁴⁷W. Qiu, T. Merckx, M. Jaysankar, C. Masse de la Huerta, L. Rakocovic, W. Zhang, U. W. Paetzold, R. Gehlhaar, L. Froyen, J. Poortmans *et al.*, "Pinhole-free perovskite films for efficient solar modules," *Energy Environ. Sci.* **9**, 484–489 (2016).
- ⁴⁸Y. Dkhissi, H. Weerasinghe, S. Meyer, I. Benesperi, U. Bach, L. Spiccia, R. A. Caruso, and Y.-B. Cheng, "Parameters responsible for the degradation of CH₃NH₃PbI₃-based solar cells on polymer substrates," *Nano Energy* **22**, 211–222 (2016).
- ⁴⁹M.-C. Jung, S. R. Raga, L. K. Ono, and Y. Qi, "Substantial improvement of perovskite solar cells stability by pinhole-free hole transport layer with doping engineering," *Sci. Rep.* **5**, 9863 (2015).
- ⁵⁰J. F. Galisteo-López, M. Anaya, M. E. Calvo, and H. Míguez, "Environmental effects on the photophysics of organic-inorganic halide perovskites," *J. Phys. Chem. Lett.* **6**, 2200–2205 (2015).
- ⁵¹D. Bryant, N. Aristidou, S. Pont, I. Sanchez-Molina, T. Chotchunangatchaval, S. Wheeler, J. R. Durrant, and S. A. Haque, "Light and oxygen induced degradation limits the operational stability of methylammonium lead triiodide perovskite solar cells," *Energy Environ. Sci.* **9**, 1655–1660 (2016).
- ⁵²B. Li, Y. Li, C. Zheng, D. Gao, and W. Huang, "Advancements in the stability of perovskite solar cells: Degradation mechanisms and improvement approaches," *RSC Adv.* **6**, 38079–38091 (2016).
- ⁵³J. Carrillo, A. Guerrero, S. Rahimnejad, O. Almora, I. Zarazua, E. Mas-Marza, J. Bisquert, and G. Garcia-Belmonte, "Ionic reactivity at contacts and aging of methylammonium lead triiodide perovskite solar cells," *Adv. Energy Mater.* **6**, 1502246 (2016).
- ⁵⁴C. Eames, J. M. Frost, P. R. F. Barnes, B. C. O'Regan, A. Walsh, and M. S. Islam, "Ionic transport in hybrid lead iodide perovskite solar cells," *Nat. Commun.* **6**, 7497 (2015).
- ⁵⁵D. W. deQuilettes, W. Zhang, V. M. Burlakov, D. J. Graham, T. Leijtens, A. Osherov, V. Bulovic, H. J. Snaith, D. S. Ginger, and S. D. Stranks, "Photo-induced halide redistribution in organic-inorganic perovskite films," *Nat. Commun.* **7**, 11683 (2016).